1 **A deep learning framework for inference of single-trial neural population activity from calcium imaging**
2 **with sub-frame temporal resolution**

3 Feng Zhu[1,2], Harrison A. Grier[3], Raghav Tandon[1], Changjia Cai[4], Andrea Giovannucci[4,5,6,*], Matthew T. Kaufman[7,8,^,*],
4 Chethan Pandarinath[1,9,10,^,*]
5
6 1. Wallace H. Coulter Department of Biomedical Engineering, Emory University and Georgia Institute of Technology, Atlanta, GA,
7   USA
8 2. Neuroscience Graduate Program, Graduate Division of Biological and Biomedical Sciences, Emory University, Atlanta, GA, USA
9 3. Committee on Computational Neuroscience, The University of Chicago, Chicago, IL, USA
10 4. Joint Biomedical Engineering Department University of North Carolina at Chapel Hill and North Carolina State University. Chapel
11   Hill, NC, USA.
12 5. Neuroscience Center, University of North Carolina at Chapel Hill. Chapel Hill, NC, USA.
13 6. Closed-Loop Engineering for Advanced Rehabilitation (CLEAR). North Carolina State University. Raleigh, NC. USA.
14 7. Department of Organismal Biology and Anatomy, The University of Chicago, Chicago, IL, USA
15 8. Neuroscience Institute, The University of Chicago, Chicago, IL, USA
16 9. Department of Neurosurgery, Emory University, Atlanta, GA, USA
17 10. Center for Machine Learning, Georgia Institute of Technology, Atlanta, GA, USA
18 ^ Authors contributed equally
19 * Correspondence: chethan [at] gatech.edu, agiovann [at] email.unc.edu, mattkaufman [at] uchicago.edu
20

21 ## Abstract:

22 In many brain areas, neural populations act as a coordinated network whose state is tied to behavior on a moment-by-
23 moment basis and millisecond timescale. Two-photon (2p) calcium imaging is a powerful tool to probe network-scale
24 computation, as it can measure the activity of many individual neurons, monitor multiple layers simultaneously, and sample
25 from identified cell types. However, estimating network states and dynamics from 2p measurements has proven challenging
26 because of noise, inherent nonlinearities, and limitations on temporal resolution. Here we describe RADICaL, a deep learning
27 method to overcome these limitations at the population level. RADICaL extends methods that exploit dynamics in spiking
28 activity for application to deconvolved calcium signals, whose statistics and temporal dynamics are quite distinct from
29 electrophysiologically-recorded spikes. It incorporates a novel network training strategy that exploits the timing of 2p
30 sampling to recover network dynamics with high temporal precision. In synthetic tests, RADICaL infers network states more
31 accurately than previous methods, particularly for high-frequency components. In real 2p recordings from sensorimotor areas
32 in mice performing a "water grab" task, RADICaL infers network states with close correspondence to single-trial variations
33 in behavior, and maintains high-quality inference even when neuronal populations are substantially reduced.
34

35 ## Introduction

36 In recent years, advances in neural recording technologies have enabled simultaneous monitoring of the activity of large
37 neural populations[1]. These technologies are enabling new insights into how neural populations implement the computations
38 necessary for motor, sensory, and cognitive processes[2]. However, different recording technologies impose distinct tradeoffs
39 in the types of questions that may be asked[3]. Modern electrophysiology enables access to hundreds to thousands of neurons
40 within and across brain areas with high temporal fidelity. Yet in any given area, electrophysiology is limited to a sparse
41 sampling of relatively active, unidentified neurons (**Fig. 1a**). In contrast, two photon (2p) calcium imaging offers the ability to
42 monitor the activity of vast populations of neurons - rapidly increasing from many tens of thousands to millions[4–6] - in 3-D,
43 often with identified layers and cell types of interest[7,8]. Thus 2p imaging is a powerful tool for understanding how neural
44 circuitry gives rise to function.
45

46 A key tradeoff, however, is that the fluorescence transients measured via 2p imaging are a low-passed and nonlinearly-
47 distorted transformation of the underlying spiking activity (**Fig. 1b**). Further, because neurons are serially scanned by a laser
48 that traverses the field of view (FOV), a trade-off exists between the size of the FOV (and hence the number of neurons
49 monitored), the sampling frequency, and the pixel size (and therefore the signal-to-noise with which each neuron is sampled).
50 These factors together limit the fidelity with which the activity of large neuronal populations can be monitored and extracted
51 via 2p, and thus limit our ability to link 2p activity to neural computation and behavior on fine timescales.
52

In recent years, a large amount of effort has been dedicated to improving the inference of spike trains from 2p data by detecting calcium influx events, *i.e.*, time points where single spikes, or multiple spikes in close succession, produce detectable fluorescence transients[9]. Ideally the spikes-to-fluorescence transformation would be invertible, such that analyzing calcium events would be equivalent to analyzing spiking activity[3]. However, recent benchmarks illustrate that a variety of algorithms to infer calcium events reach a similar ceiling of performance and make consistent predictions, and all achieve limited correspondence to ground truth spiking activity obtained with electrophysiology, particularly on fine timescales[10,11]. Comparisons of calcium imaging and electrophysiology suggest that the two methods may therefore lead to divergent scientific findings[3,12–14], largely due to limitations when inferring spikes from calcium traces.

Rather than focusing on the responses of individual neurons, an alternative approach is to characterize patterns of covariation across a neuronal population to reveal the internal state of the underlying network. These "latent variable models", or simply "latent models", describe each neuron's activity as a reflection of the network's state. For example, when applied to electrophysiological data, latent models assume that an individual neuron's spiking is a noisy observation of a latent "firing rate", which fluctuates in a coordinated way with the firing rates of other neurons in the population. Despite their abstract nature, the network states inferred by latent models can reveal key insights into the computations being performed by the brain areas of interest[2]. Inferred network states can also enhance our ability to relate neural activity to behavior. For example, one state-of-the-art deep learning method to estimate network states from electrophysiological spiking data is Latent Factor Analysis via Dynamical Systems (LFADS)[15,16]. In applications to data from motor, sensory, and cognitive regions, LFADS reveals rules that govern how network states progress over time and that are consistent across behavioral conditions, while also revealing tight correspondences with single-trial behavior on a millisecond timescale[16,17].

Given the success of latent models in uncovering network states from electrophysiological data, here we test whether such models can achieve accurate inference of network states from activity monitored through 2p calcium imaging. We first begin with LFADS, and evaluate network state inference using simulated 2p data in which activity reflects known, nonlinear dynamical systems, and with real 2p data from mice performing a water reaching task. LFADS uncovers network state with substantially higher accuracy then standard approaches (e.g., deconvolution plus Gaussian smoothing). We then develop and test a new approach, the Recurrent Autoencoder for Discovering Imaged Calcium Latents (RADICaL), to further improve inference over LFADS. RADICaL extends LFADS with innovations tailored specifically for 2p data. In particular, we modify the network architecture to better account for the statistics of deconvolved calcium signals, and develop a novel network training strategy that exploits the staggered timing of 2p sampling of neuronal populations to achieve subframe temporal resolution. Our new approach substantially improves inference of network states from 2p data, shown in synthetic data through accurate recovery of high-frequency features (up to 20 Hz), and in real data through improved prediction of neuronal activity, as well as prediction of single-trial variability in hand kinematics during rapid reaches (lasting 200-300 ms). Ultimately, RADICaL provides an avenue to tie precise, population-level descriptions of neural computation with the anatomical and circuit details revealed via calcium imaging.

Results

Leveraging population dynamics to infer network states from 2p imaging data

Dynamical systems models such as LFADS rely on two key principles to infer network states from neural population activity. First, simultaneously recorded neurons exhibit coordinated spatial patterns of activation that reflect the state of the network[18,19]. Due to this coordination, network states might be reliably estimated even if the measurement of individual neurons' activity is unreliable. Second, these coordinated spatial patterns evolve over time based on consistent rules (dynamics)[2,20]. Thus, while it may be challenging to accurately estimate the network's state based on activity at a single time point, knowledge of the network's dynamics provides further information to help constrain network state estimates using data from multiple time points.

To apply these principles to improve inference from 2p data, we extended LFADS to produce RADICaL (**Fig. 1c**). Both LFADS and RADICaL model neural population dynamics using recurrent neural networks (RNNs) in a sequential autoencoder configuration (details in *Methods*, and in previous work[15,16]). This configuration is built on the assumption that the network states underlying neural population activity can be approximated by an input-driven dynamical system, and that observed activity is a noisy observation of the state of the dynamical system. The dynamical system itself is modeled by an

104 RNN (the 'generator'). For any given trial, the time-varying network states can be captured by three pieces of information:
105 the initial state of the dynamical system (trial-specific), the dynamical rules that govern state evolution (shared across trials),
106 and any external inputs that may affect the dynamics (trial-specific). The states of the generator are linearly mapped onto a
107 latent space to produce a 'factors' representation, which is then transformed to produce the time-varying output for each
108 neuron (detailed below). The model has a variety of hyperparameters that control training and prevent overfitting, whose
109 optimal settings are not known *a priori*. To ensure that these hyperparameters were optimized properly for each dataset, we
110 built RADICaL on top of a powerful, large-scale hyperparameter optimization framework we recently developed known as
111 AutoLFADS[17,21].

112

113 **Novel features of RADICaL**
114 RADICaL incorporates two major innovations over LFADS and AutoLFADS. First, we modified RADICaL's observation model
115 to better account for the statistics of deconvolved events. In LFADS, discrete spike count data are modeled as samples from
116 an underlying time-varying Poisson process for each neuron. However, deconvolving 2p calcium signals results in
117 continuous-valued, time-varying events, with limited correspondence to the actual spike times[10]. In RADICaL, deconvolved
118 events are therefore modeled as samples from a time-varying zero-inflated gamma (ZIG) distribution, which has been shown
119 to be more appropriate for calcium data[22], and whose parameters are taken as the output of the generator RNN (**Fig. 1c**;
120 details in *Methods*). We then define the network state at any given time point as a vector containing the inferred (i.e., de-
121 noised) event rates of all neurons, where the de-noised event rate is taken as the mean of each neuron's inferred ZIG
122 distribution at each time point. The de-noised event rates are latent variables that are tied to the underlying network state at
123 each time point. We note that in RADICaL, the generator RNN must produce multiple parameters that control the shape of
124 the ZIG distributions, which may result in activity at the level of the generator and factors that does not directly correspond
125 to the biological network's activity. To avoid this complication, rather than using the factors as an estimate of the biological
126 network's state, we used the de-noised event rates. Doing so for both RADICaL and AutoLFADS allowed us to compare
127 methods as directly as possible.

128

129 Second, we developed a novel neural network training strategy, selective backpropagation through time (SBTT), that
130 leverages the precise sampling times of individual neurons to enable recovery of high-frequency network dynamics. Since
131 standard multiphoton acquisition systems rely on point-by-point raster scanning of a laser beam to acquire frames, it is
132 possible to increase temporal precision of individual neurons' sample times beyond the timing of individual frames, by
133 exploiting the relationship between scanning position and accumulated scanning time within the frame (**Fig. 1d**). To leverage
134 this information to improve inference of high-frequency network dynamics on single trials, we reframe the underlying
135 interpolation problem as a missing data problem: we treat low-sampling rate data from each neuron as high-sampling rate
136 data at the level of the population. In this framing, each neuron is effectively sampled sparsely in time, *i.e.*, the majority of
137 time points for each neuron do not contain valid data (**Fig. 1e**). Such sparsely sampled data creates a challenge when
138 training the underlying neural network: briefly, neural networks are trained by adjusting their parameters (weights), and
139 performing this adjustment requires evaluating the gradient of a cost function with respect to weights. SBTT allows us to
140 compute this gradient using only the valid data, and ignore the many missing samples (**Fig. 1f**; see *Methods*). Because this
141 feature only affects how we compute the gradient and update the weights, the network still infers event rates for every neuron
142 at every time point, regardless of whether samples exist at that time point or not. This allows the trained network to accept
143 sparsely-sampled observations as input, and produce high-temporal resolution event rate estimates at its output.
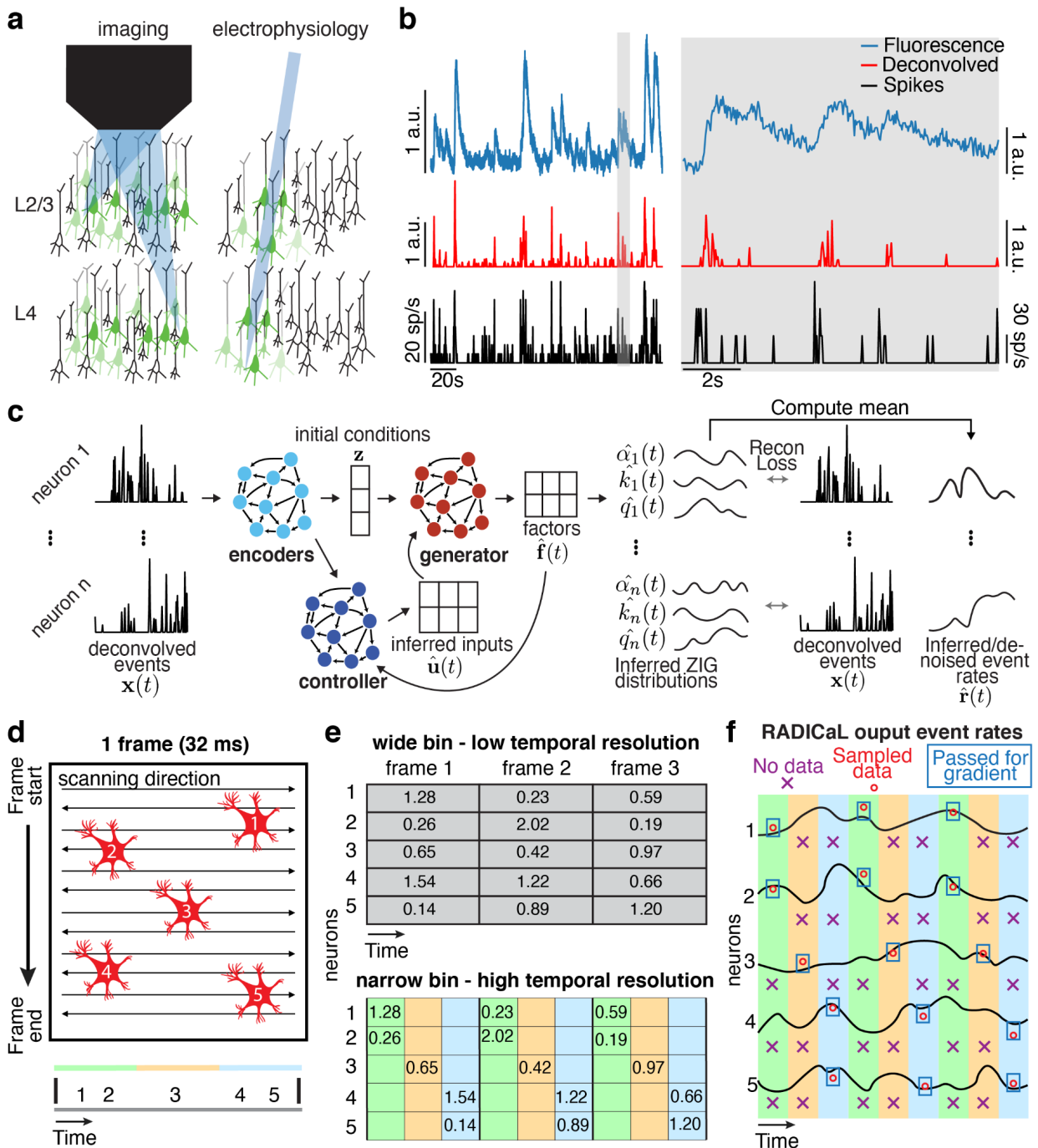
Figure 1 | Improving inference of network states from 2p imaging. (a) Calcium imaging offers the ability to monitor the activity of hundreds or thousands of neurons, in 3-D, often with cell types of interest and layers identified. In contrast, electrophysiology sparsely samples the neurons in the vicinity of a recording electrode, and may be biased toward neurons with high firing rates. (b) 2p fluorescence transients are a low-passed and lossy transformation of the underlying spiking activity. Spike inference methods may provide a reasonable estimate of neurons' activity on coarse timescales (*left*), but yield poor estimates on fine timescales (*right*; data from ref. [23]). (c) RADICaL uses a recurrent neural network-based generative model to infer network states - *i.e.,* de-noised event rates for the population of neurons - and assumes a time-varying ZIG observation model. (d) *Top*: in 2p imaging, the laser's serial scanning results in different neurons being sampled at different times within the frame. *Bottom*: individual neurons' sampling times are known with sub-frame precision (colors) but are typically analyzed with whole-frame precision (grey). (e) Sub-frame binning precisely captures individual neurons' sampling times but results in neuron-time points without data. The numbers in the table indicate the deconvolved event in each frame. (f) SBTT is a novel network training method for sparsely sampled data that prevents unsampled time-neuron data points from affecting the gradient computation.

RADICaL uncovers high-frequency features from simulated data

159 We first tested RADICaL using simulated 2p data, which provides a valuable tool for quantifying performance because the
160 underlying network states are known and are parameterizable. We hypothesized that the new features of RADICaL would
161 allow it to infer high-frequency features with greater accuracy than standard approaches, such as Gaussian-smoothing the
162 deconvolved events ("s-deconv") or the simulated fluorescence traces themselves ("s-sim-fluor"), or state-of-the-art tools for
163 electrophysiology analysis, such as AutoLFADS. We generated synthetic spike trains by simulating a population of neurons
164 whose firing rates were linked to the state of a Lorenz system[15,24] (detailed in *Methods* and **Supp. Fig. 1a**). We ran the
165 Lorenz system at various speeds, allowing us to investigate the effects of temporal frequency on the quality of network state
166 recovery achieved by different methods. In the 3-dimensional Lorenz system, the *Z* dimension contains the highest-
167 frequency content (**Supp. Fig. 1b**). Here we denote the frequency of each Lorenz simulation by the peak frequency of the
168 power spectrum of its *Z* dimension (**Supp. Fig. 1c**).
169
170 We used the synthetic spike trains to generate realistic noisy fluorescence signals consistent with GCAMP6f (detailed in
171 *Methods* and **Supp. Fig. 2**). To recreate the variability in sampling times due to 2p laser scanning, fluorescence traces were
172 simulated at 100 Hz and then sub-sampled at 33.3 Hz, with offsets in each neuron's sampling times consistent with spatial
173 distributions across a simulated FOV. We then deconvolved the generated fluorescence signals to extract events [25,26].
174 Because RADICaL uses SBTT, it could be applied directly to the deconvolved events with offset sampling times. In contrast,
175 for both AutoLFADS and s-deconv, deconvolved events for all neurons were treated as all having the same sampling times
176 (i.e., consistent with the frame times), as is standard in 2p imaging (detailed in *Methods*).
177
178 Despite the distortion introduced by the fluorescence simulation and deconvolution process, RADICaL was able to infer
179 event rates that closely resembled the true underlying rates (**Fig. 2a**). To assess whether each method accurately inferred
180 the time-varying state of the Lorenz system, we mapped the representations from the different approaches - i.e., the event
181 rates inferred by RADICaL or AutoLFADS, the smoothed deconvolved events, and the smoothed simulated fluorescence
182 traces - onto the true underlying Lorenz states using ridge regression. We then quantified performance using the coefficient
183 of determination (R^2), which quantifies the fraction of the variance of the true latent variables captured by the estimates.
184 **Figure 2b** shows the Lorenz *Z* dimension for example trials from three Lorenz speeds, as well as the recovered values for
185 three of the methods. RADICaL inferred latent states with high fidelity ($R^2 > 0.8$) up to 15 Hz, and significantly outperformed
186 other methods across a range of frequencies (**Fig. 2c**; performance for the *X* and *Y* dimensions is shown in **Supp. Fig. 3**;
187 $p < 0.05$ for all frequencies and dimensions, paired, one-sided t-Test, detailed in *Methods*).

188
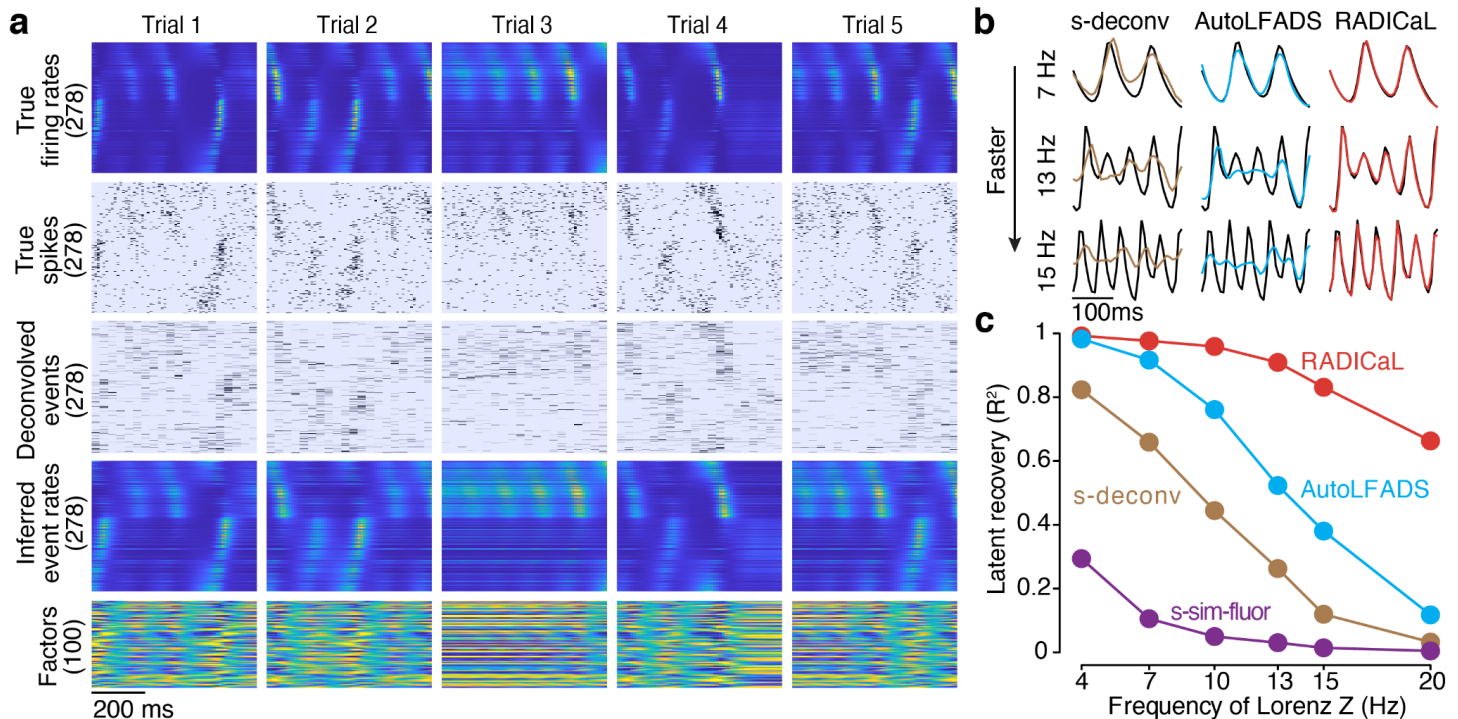
Figure 2 | Application of RADICaL to synthetic data. (a) Example firing rates and spiking activity from a Lorenz system simulated at 7
Hz, deconvolved calcium events (inputs to RADICaL), and the corresponding rates and factors inferred by RADICaL. Simulation
parameters were tuned so that the performance in inferring spikes using OASIS matched previous benchmarks[10] (see *Methods*). (b) True

192 and inferred Lorenz latent states (*Z* dimension) for a single example trial from Lorenz systems simulated at three different frequencies.
193 Black: true. Colored: inferred. (c) Performance in estimating the Lorenz *Z* dimension as a function of simulation frequency was quantified
194 by variance explained (R^2) for all 4 methods.

196 These synthetic results provide an important proof-of-principle that RADICaL can infer high-frequency features of the network
197 activity underlying 2p signals, which is readily validated when ground truth is known. However, it is important to acknowledge
198 limitations of the simulation process that might constrain the generality of these results when applying to real data. In
199 particular, the parameter space is very large, especially considering the variety of calcium indicators, protein expression
200 patterns, imaging settings, cell types and firing rate patterns. An exhaustive search of this parameter space is infeasible,
201 and we chose parameters so that the resulting signal-to-noise regime produced similar correlations between real and inferred
202 spike trains as those typically observed[10] (see *Methods*). However, it is difficult to know whether the results from any
203 particular choice of simulation parameters (or a variety of choices) can be extrapolated to real experimental conditions. Thus,
204 we next benchmarked performance on real data to demonstrate RADICaL's utility in the real world.

206 **RADICaL improves network state inference in data from a mouse water grab task**
207 We next tested RADICaL on 2p recordings from mice performing a forelimb water grab task (**Fig. 3a**, *top*). We analyzed data
208 from four experiments: two mice, and two sessions from each mouse in which different brain areas were imaged (M1, S1).
209 Our task is a variant of the water-reaching task of Galiñanes & Huber[27]. In each trial, the mouse was cued by the pitch of an
210 auditory tone to reach to a left or right spout and retrieve a droplet of water with its right forepaw (**Fig. 3a**, *bottom*; see
211 *Methods*). The forepaw position was tracked at 150 frames per second with DeepLabCut[6] for 420-560 trials per experiment.
212 To test whether each method could reveal structure in the neural activity at finer resolution than left vs. right reaches, we
213 divided trials from each condition into subgroups based on forepaw height during the reach (**Fig. 3a**, *top right*; see *Methods*).
214 Two-photon calcium imaging from GCaMP6f transgenic mice was performed at 31 Hz, with 430-510 neurons within the FOV
215 in each experiment (**Fig. 3b**).

217 With real datasets, a key challenge when benchmarking latent variable inference is the lack of ground truth data for
218 comparison. A useful first-order assessment is whether the event rates inferred for individual trials match the empirical peri-
219 stimulus time histograms (PSTHs), *i.e.*, the rates computed by averaging noisy single-trial data across trials with similar
220 behavioral characteristics[16,17]. While this approach obscures meaningful across-trial variability, it provides a 'de-noised'
221 estimate that is useful for coarse performance quantification and comparisons. To compute empirical PSTHs, we averaged
222 the smoothed deconvolved events (s-deconv rates) across trials within each subgroup.

224 We found that RADICaL-inferred event rates recapitulated features of individual neurons' activity that were apparent in the
225 empirical PSTHs, both when averaging across trials, but also on individual trials (**Fig. 3c**). Importantly, RADICaL is an
226 unsupervised method, meaning that it was not provided any behavioral information, such as whether the mouse reached to
227 the left or right on a given trial, or which subgroup a trial fell into. Yet the single-trial event rates inferred by RADICaL showed
228 clear separation not only between left and right reach conditions, but also between subgroups of trials within each condition.
229 This separation was not clear with the single-trial s-deconv rates. We quantified the correspondence between the single-trial
230 inferred event rates and the empirical PSTHs via Pearson's correlation coefficient (*r*; see *Methods*). RADICaL single-trial
231 event rates showed substantially higher correlation with the empirical PSTHs than s-deconv rates (**Fig. 3d**) or those inferred
232 by AutoLFADS (**Supp. Fig. 4**). Importantly, these improvements were not limited to a handful of neurons, but instead were
233 broadly distributed across the population.

235 We next tested whether the population activity inferred by RADICaL also showed meaningful structure on individual trials.
236 We produced low-dimensional visualizations of the population's activity by applying principal component analysis (PCA) to
237 the RADICaL-inferred or s-deconv event rates after log-transforming and trial-averaging, and then projected the single-trial
238 event rates (also log-transformed) into the subspace formed by the top three PCs. The low-D trajectories computed from the
239 RADICaL-inferred rates showed consistent, clear single-trial structure that corresponded to behavioral conditions and
240 subgroups for all four experiments (**Fig. 3e**, *top row*; **Supp. Fig. 5**, *top row*), despite RADICaL receiving no direct information
241 about which trials belonged to which condition. In comparison, low-D trajectories computed from the s-deconv rates showed
242 noisy single-trial structure with little correspondence to behavioral subgroups (**Fig. 3e**, *bottom row*; **Supp. Fig. 5**, *bottom*
243 *row*).
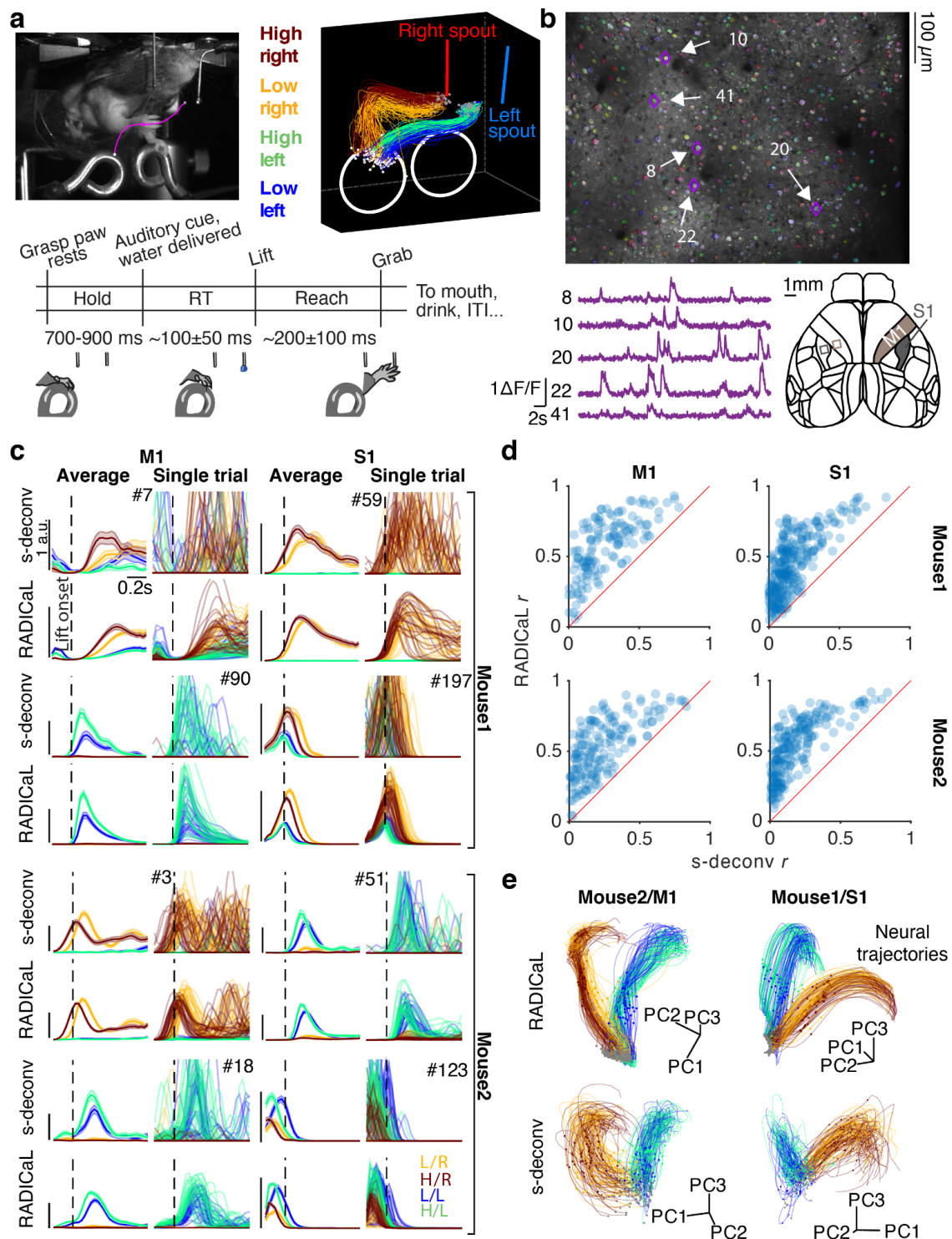
Figure 3 | Application of RADICaL to real two-photon calcium imaging of a water grab task. (a) Task. *Top left*: Mouse performing the water grab task. Pink trace shows paw centroid trajectory. Bottom: Event sequence/task timing. RT: reaction time. ITI: inter-trial interval. *Top right*: Individual reaches colored by subgroup identity. (b) *Top*: an example field of view (FOV), identified neurons colored randomly. *Bottom left*: dF/F from a single trial for 5 example neurons. *Bottom right*: Allen Atlas M1/S1 brain regions imaged. (c) Comparison of trial-averaged (left) and single-trial (right) rates for 8 individual neurons for two different brain areas (left vs. right) and two different mice (top half vs. bottom half) for s-deconv and RADICaL (alternating rows). *Left*: each trace represents a different reach subgroup (4 in total) with error bars indicating s.e.m. *Right*: each trace represents an individual trial (same color scheme as trial-averaged panels). *Odd rows*: s-deconv event rates (Gaussian kernel: 40 ms s.d.). *Even rows*: RADICaL-inferred event rates. Horizontal scale bar represents 200 ms. Vertical scale bar denotes event rate (a.u.). Vertical dashed line denotes lift onset time. (d) Performance of RADICaL and s-deconv in capturing the empirical PSTHs on single trials. Correlation coefficient r was computed between the inferred single-trial event rates and empirical PSTHs. Each point represents an individual neuron. (e) Single-trial neural trajectories derived from RADICaL

256 rates (top row) and s-deconv rates (bottom row) for two experiments (*left*: Mouse2 M1; *right*: Mouse1 S1), colored by subgroups. Each
257 trajectory is an individual trial, plotting from 200 ms before to 400 ms after lift onset. Lift onset times are indicated by the dots in the same
258 colors with the trajectories. Grey dots indicate 200 ms prior to lift onset time. Neural trajectories from additional experiments are shown
259 in **Supp. Fig. 5**.

261 **RADICaL captures dynamics that improve hand kinematics prediction**
262 We next tested whether the RADICaL-inferred event rates were closely linked to behavior by decoding forepaw positions
263 and velocities from the inferred event rates using cross-validated ridge regression (**Fig. 4a**). Decoding using RADICaL-
264 inferred rates significantly outperformed results from s-deconv rates, or from the AutoLFADS-inferred rates (**Fig. 4b**; position:
265 average R^2 of 0.90 across all experiments, versus 0.72 and 0.83 for s-deconv and AutoLFADS, respectively; velocity:
266 average R^2 of 0.59 across the mice/areas, versus 0.32 and 0.45 for s-deconv and AutoLFADS, respectively; $p<0.05$ for
267 position and velocity for all individual experiments, paired, one-sided t-test, detailed in *Methods*). Importantly, the
268 performance advantage was not achieved by simply predicting the mean event rates for all trials of a given condition:
269 RADICaL also outperformed AutoLFADS and s-deconv in decoding the kinematic residuals (i.e., the single-trial deviations
270 from the mean; **Supp. Fig. 7**). To assess how these decoding improvements were distributed as a function of frequency, we
271 computed the coherence between the true and decoded positions and velocities for each method (**Fig. 4c**). RADICaL
272 predictions showed higher coherence with behavior than predictions from s-deconv or AutoLFADS across a wide range of
273 frequencies, and the difference in coherence between RADICaL and AutoLFADS widened (especially for position) at higher
274 frequencies (5-15 Hz). Notably, decoding was improved due to both innovations in RADICaL (i.e., modeling events with a
275 ZIG distribution, and SBTT), and the combination of the two innovations significantly improved performance over each
276 innovation alone (**Supp. Fig. 8**).
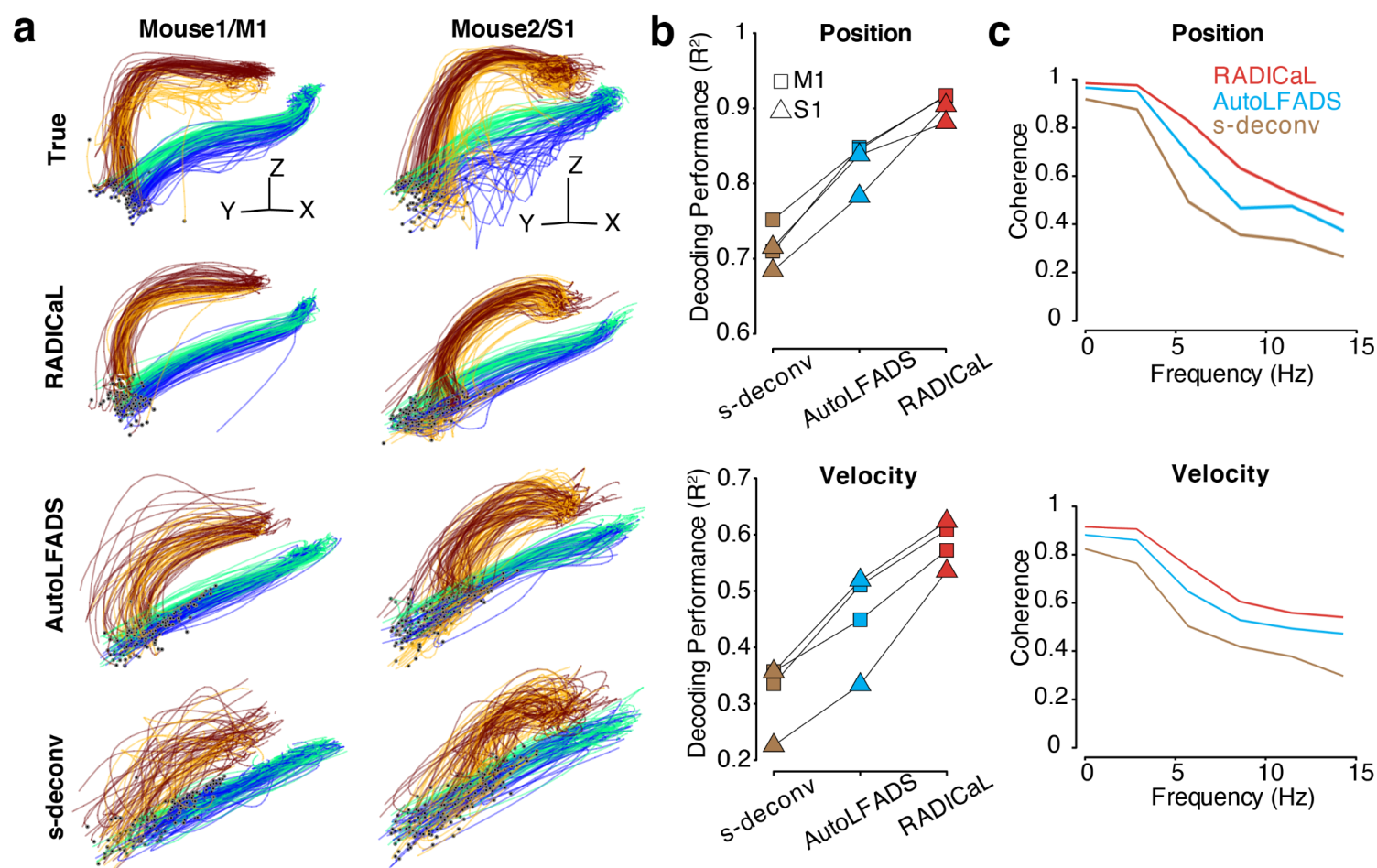
Figure 4 | RADICaL improves prediction of behavior. (a) Decoding hand kinematics using ridge regression. Each column shows an
example mouse/area. Row 1: true hand positions trajectories, colored by subgroups. Rows 2–4: predicted hand positions using ridge
regression applied to the event rates inferred by RADICaL or AutoLFADS, or s-deconv rates (Gaussian kernel: 40 ms s.d.). Hand positions
from additional experiments are shown in **Supp. Fig. 6**. (b) Decoding accuracy was quantified by measuring variance explained (R^2)
between the true and decoded position (top) and velocity (bottom) across all trials across each of the 4 datasets (2 mice for M1, denoted

283   by squares, and 2 mice for S1, denoted by triangles), for all 3 techniques. (c) Quality of reconstructing the kinematics across frequencies
284   was quantified by measuring coherence between the true and decoded position (top) and velocity (bottom) for individual trials across all
285   4 datasets, for all 3 techniques.

RADICaL retains high decoding performance when reducing the number of neurons used in the model

288   In previous demonstrations on electrophysiological spiking data, LFADS maintained accurate performance in reconstructing
289   single-trial neural activity and decoding even when reducing the number of sampled neurons[16]. Enabling the same
290   capabilities for 2p imaging could help mitigate the effects of the tradeoffs in sampling frequency or signal-to-noise that occur
291   when laser scanning over large FOVs. To evaluate whether this holds for RaDICAL, we performed a neuron-downsampling
292   experiment where we gradually reduced the number of neurons used in training RADICaL or AutoLFADS (**Fig. 5a**). RADICaL
293   retained relatively high decoding performance as the population size was reduced (**Fig. 5b**; data from Mouse2 M1). Decoding
294   performance declined gradually, with a steeper slope for velocity. Notably, however, performance when only 121/439
295   neurons were used for training RADICaL was similar to that of AutoLFADS - and higher than for s-deconv - even when those
296   methods were applied to the full population of 439 neurons. Note that this analysis represents a lower bound on performance:
297   for this proof-of-concept, we simply artificially excluded from our analysis data collected as the laser scanned outside the
298   restricted FOVs, which resulted in substantial time periods that lacked data entirely (e.g., 2/3 of the total sampling time for
299   the smallest FOV considered). In a real application, those time periods that were artificially excluded could instead be used
300   to monitor other brain areas or layers, or to monitor the same neurons with higher sampling rates, either of which might be
301   expected to provide additional information. These results provide an avenue to retain information by scanning smaller areas
302   when capturing multiple layers or regions, opening opportunities to study interesting questions such as communication
303   between layers or interactions between regions (see *Discussion*).
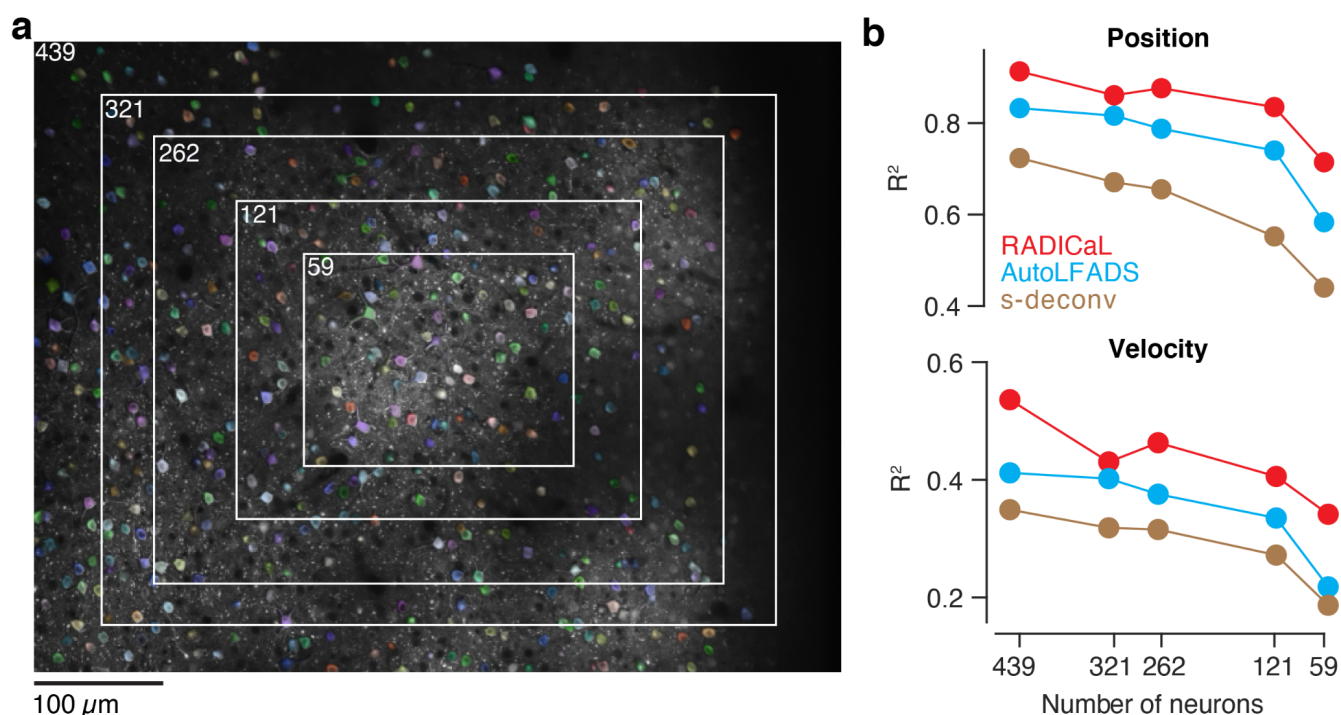
Figure 5 | RADICaL retains high decoding performance in a neuron downsampling experiment. (a) The area selected to include
was gradually shrunk to the center of the FOV to reduce the number of neurons included in training RADICaL or AutoLFADS. (b) Decoding
performance measured using variance explained (R^2) as a function of the number of neurons used in each technique (top: Position;
bottom: Velocity). Data from Mouse2 M1.

Discussion

311   2p imaging is a widely-used method for interrogating neural circuits, with the potential to monitor vast volumes of neurons
312   and provide new circuit insights that elude electrophysiology. To date, however, it has proven challenging to precisely infer
313   network states from imaging data, due in large part to the inherent noise, indicator dynamics, and low temporal resolution
314   associated with 2p imaging. RADICaL bridges this gap. RADICaL is tailored specifically for 2p imaging, with a noise

emissions model that is appropriate for deconvolved calcium events, and a novel network training strategy (SBTT) that takes advantage of the specifics of 2p laser scanning to achieve substantially higher temporal resolution. Through synthetic tests, we demonstrated that RADICaL accurately infers network states and substantially outperforms alternate approaches in uncovering high-frequency fluctuations. Then, through careful validation on real 2p data, we demonstrated that RADICaL infers network states that are closely linked to single-trial behavioral variability, even on fast timescales. Finally, we demonstrated that RADICaL maintains high-quality inference of network states even as the neural population size is reduced substantially.

The ability to de-noise neural activity on single trials is especially valuable. First, de-noising improves the ability to decode behavioral information from neural activity, allowing subtle relationships between neural activity and behavior to be revealed (**Fig. 4**). Second, de-noising may enable the field to move away from experimental paradigms that evoke the stereotyped behaviors that are needed to facilitate trial-averaging of neural data. This support for reduced stereotypy could allow greater insight in experiments with animals such as mouse and marmoset, where powerful experimental tools are available but highly repeatable behaviors are challenging to achieve. A move away from trial-averaging could also enable better interpretability of more complex or naturalistic behaviors[17,28–31]. Third, this de-noising capability will enable greater insight into processes that fundamentally differ from trial to trial, such as learning from errors[32,33], variation in internal states such as arousal[34,35], or paradigms in which tuning to uninstructed movements contaminates measurement of the task-related behavioral variables of interest[36]. Finally, this de-noising also reverses some of the distortions of neural activity introduced by calcium imaging, enabling greatly improved inference of neural dynamics (**Fig. 2**) when compared with known failures using imaging data[3].

In recent years, a variety of computational methods have been developed to analyze 2p imaging data[9]. 2p preprocessing pipelines[5,26] normally include methods that correct for motion, localize and demix neurons' fluorescence signals, and infer event rates from fluorescence traces. Several studies have applied deep learning in attempts to improve signal quality[37–39], while a few others have focused on uncovering population-level structure[40–45] or locally linear dynamics underlying population activity, in particular via switching linear dynamical systems-based methods[46,47]. Here we build RADICaL on the AutoLFADS architecture, which leverages deep learning and large-scale distributed training. This enables the integration of more accurate observation models (ZIG) and powerful optimization strategies (SBTT), while potentially inheriting the high performance and generalized applicability previously demonstrated for AutoLFADS[17].

Many behaviors are performed on fast timescales (e.g., saccades, reaches, movement correction, etc), and thus previous work has made steps in overcoming the limits of modest 2p frame rates in attempts to infer the fast changes in neural firing rates that relate to these fast behaviors. Efforts to chip away at this barrier have relied on regularities imposed by repeated stimuli or highly stereotyped behavior[48,49], or jittered inferred events on sub-frame timescales to minimize the reconstruction error of the associated fluorescence[37]. RADICaL takes a different approach. In particular, it links subframe timing to neural population dynamics, representing a more powerful and generalizable approach that does not require stereotypy in the behavior or neural response and which could therefore be applied to datasets with more naturalistic or flexible behaviors.

Though we made an effort to test with realistic simulations and on real 2p data from both M1 and S1, it remains untested how RADICaL would generalize to other experimental settings. Noise level can span a wide range in real experiments, depending on the optics, calcium indicators, expression levels, and other factors. Behaviors can vary in complexity and population dynamics can be high-dimensional. Though it is not guaranteed that RADICaL would work in all possible settings, it provides a solution to the spatiotemporal tradeoff that is inherent to any scanning technique, which enables retaining temporal resolution while increasing the spatial area of sampling.

While RADICaL operates on deconvolved calcium events, future work to eliminate this deconvolution step may allow further improvements in temporal resolution. Because deconvolution outputs an event rate for each frame - which is a summary of the cumulative effect of the spikes within the frame - it necessarily discards some high-frequency features in the data. Instead it may be possible to build an end-to-end model that integrates the generative rates-to-fluorescence process and operates on the fluorescence traces directly. Complementary work has begun exploring in this direction[50], but our unique innovation of selective backprop through time presents an opportunity to greatly improve the quality of recovering high-frequency features when the sampling rate is limited. More broadly, carefully-designed benchmarking efforts for network state inference

367 from 2p data could provide an invaluable resource for systematically comparing methods and building on advances from
368 various different developers.
369
370 The ability to achieve high-quality network state inference despite limited neuronal population size opens the door to testing
371 new choices about how to scan during the experiments themselves, e.g., by scanning smaller and more disparate FOVs
372 (across layers[7,8] or brain areas[51,52]) to understand how spatially-segregated populations interact, while potentially preserving
373 the ability to infer network states from each FOV. When the number of neurons within each FOV is limited, one advantage
374 that RADICaL inherits from LFADS is that it allows for multi-session stitching[16], which could provide an avenue to combine
375 data from different sessions to improve inference of the underlying dynamics for each FOV.
376
377 In sum, RADICaL provides a framework to push back the limits of the space-time tradeoff in 2p calcium imaging, enabling
378 accurate inference of population dynamics in vast populations and with identified neurons. Future work will explore how best
379 to exploit these capabilities for different experimental paradigms, and to link the power of dynamics with the anatomical detail
380 revealed with calcium imaging.
381

Acknowledgements

391

Code availability

393 Code will be made available upon publication.
394

Data availability

396 Data will be made available upon reasonable request at the time of publication.
397

Author Contributions

399 F.Z. and C.P. designed the study, with input from A.G. and M.K.. C.P. and M.T.K. conceptualized the SBTT approach.
400 F.Z. and C.P. performed analyses and wrote the manuscript with input from all other authors. F.Z. and C.P. developed
401 the algorithmic approach. F.Z., C.C., and A.G. developed the simulation pipeline. H.G. and M.K. designed and performed
402 experiments with mice, and developed the real data preprocessing pipeline with input from F.Z. and C.P.. R.T. contributed
403 to initial simulations and data analysis. F.Z., A.G., M.K., and C.P. edited and revised the manuscript with input from all
404 other authors.
405

References

406
407 1. Stevenson, I. H. & Kording, K. P. How advances in neural recording affect data analysis. *Nat Neurosci* **14**,
408   139–142 (2011).
409 2. Vyas, S., Golub, M. D., Sussillo, D. & Shenoy, K. V. Computation Through Neural Population Dynamics.
410   *Annual Review of Neuroscience* **43**, 249–275 (2020).
411 3. Wei, Z. *et al.* A comparison of neuronal population dynamics measured with calcium imaging and
412   electrophysiology. *PLoS computational biology* **16**, e1008198 (2020).
413 4. Demas, J. *et al. Volumetric Calcium Imaging of 1 Million Neurons Across Cortical Regions at Cellular
414   Resolution using Light Beads Microscopy*. http://biorxiv.org/lookup/doi/10.1101/2021.02.21.432164 (2021)
415   doi:10.1101/2021.02.21.432164.
416 5. Pachitariu, M. *et al.* Suite2p: beyond 10,000 neurons with standard two-photon microscopy. *BioRxiv*

417 (2017).

418 6. Peron, S. P., Freeman, J., Iyer, V., Guo, C. & Svoboda, K. A cellular resolution map of barrel cortex activity
419   during tactile behavior. *Neuron* **86**, 783–799 (2015).
420 7. Chen, J. L., Carta, S., Soldado-Magraner, J., Schneider, B. L. & Helmchen, F. Behaviour-dependent
421   recruitment of long-range projection neurons in somatosensory cortex. *Nature* **499**, 336–340 (2013).
422 8. Chen, S. X., Kim, A. N., Peters, A. J. & Komiyama, T. Subtype-specific plasticity of inhibitory circuits in
423   motor cortex during motor learning. *Nature neuroscience* **18**, 1109–1115 (2015).
424 9. Pnevmatikakis, E. A. Analysis pipelines for calcium imaging data. *Current Opinion in Neurobiology* **55**, 15–
425   21 (2019).
426 10. Berens, P. *et al.* Community-based benchmarking improves spike rate inference from two-photon calcium
427   imaging data. *PLoS computational biology* **14**, e1006157 (2018).
428 11. Pachitariu, M., Stringer, C. & Harris, K. D. Robustness of spike deconvolution for neuronal calcium
429   imaging. *Journal of Neuroscience* **38**, 7976–7985 (2018).
430 12. Evans, M. H., Petersen, R. S. & Humphries, M. D. On the use of calcium deconvolution algorithms in
431   practical contexts. *bioRxiv* 871137 (2019).
432 13. Huang, L. *et al.* Relationship between simultaneously recorded spiking activity and fluorescence signal in
433   GCaMP6 transgenic mice. *eLife* **10**, e51675 (2021).
434 14. Siegle, J. H. *et al.* Reconciling functional differences in populations of neurons recorded with two-photon
435   imaging and electrophysiology. *bioRxiv* (2020).
436 15. Sussillo, D., Jozefowicz, R., Abbott, L. & Pandarinath, C. LFADS-latent factor analysis via dynamical
437   systems. *arXiv preprint arXiv:1608.06315* (2016).
438 16. Pandarinath, C. *et al.* Inferring single-trial neural population dynamics using sequential auto-encoders. *Nat*
439   *Methods* **15**, 805–815 (2018).
440 17. Keshtkaran, M. R. *et al.* A large-scale neural network training framework for generalized estimation of
441   single-trial population dynamics. *bioRxiv* (2021).
442 18. Cunningham, J. P. & Yu, B. M. Dimensionality reduction for large-scale neural recordings. *Nat Neurosci*
443   **17**, 1500–1509 (2014).
444 19. Pandarinath, C. *et al.* Latent Factors and Dynamics in Motor Cortex and Their Application to Brain–
445   Machine Interfaces. *J. Neurosci.* **38**, 9390–9401 (2018).
446 20. Shenoy, K. V., Sahani, M. & Churchland, M. M. Cortical Control of Arm Movements: A Dynamical Systems
447   Perspective. *Annu. Rev. Neurosci.* **36**, 337–359 (2013).
448 21. Keshtkaran, M. R. & Pandarinath, C. Enabling hyperparameter optimization in sequential autoencoders for
449   spiking neural data. in *Advances in Neural Information Processing Systems* 15937–15947 (2019).
450 22. Wei, X.-X. *et al.* A zero-inflated gamma model for deconvolved calcium imaging traces. *arXiv preprint*
451   *arXiv:2006.03737* (2020).
452 23. Chen, T.-W. *et al.* Ultrasensitive fluorescent proteins for imaging neuronal activity. *Nature* **499**, 295–300
453   (2013).
454 24. Zhao, Y. & Park, I. M. Variational latent gaussian process for recovering single-trial dynamics from
455   population spike trains. *Neural computation* **29**, 1293–1316 (2017).
456 25. Friedrich, J., Zhou, P. & Paninski, L. Fast online deconvolution of calcium imaging data. *PLoS Comput Biol*
457   **13**, e1005423 (2017).
458 26. Giovannucci, A. *et al.* CaImAn an open source tool for scalable calcium imaging data analysis. *eLife* **8**,
459   e38173 (2019).
460 27. Galiñanes, G. L., Bonardi, C. & Huber, D. Directional reaching for water as a cortex-dependent behavioral
461   framework for mice. *Cell reports* **22**, 2767–2783 (2018).
462 28. Hatsopoulos, N. G., Xu, Q. & Amit, Y. Encoding of movement fragments in the motor cortex. *Journal of*
463   *Neuroscience* **27**, 5105–5114 (2007).
464 29. Krakauer, J. W., Ghazanfar, A. A., Gomez-Marin, A., MacIver, M. A. & Poeppel, D. Neuroscience needs
465   behavior: correcting a reductionist bias. *Neuron* **93**, 480–490 (2017).
466 30. Whishaw, I. Q. *et al.* Organization of the reach and grasp in head-fixed vs freely-moving mice provides
467   support for multiple motor channel theory of neocortical organization. *Experimental brain research* **235**,
468   1919–1932 (2017).
469 31. Wiltschko, A. B. *et al.* Revealing the structure of pharmacobehavioral space through motion sequencing.
470   *Nature neuroscience* **23**, 1433–1443 (2020).

32. Herzfeld, D. J., Kojima, Y., Soetedjo, R. & Shadmehr, R. Encoding of error and learning to correct that error by the Purkinje cells of the cerebellum. *Nature neuroscience* **21**, 736–743 (2018).

33. Vyas, S., O'Shea, D. J., Ryu, S. I. & Shenoy, K. V. Causal role of motor preparation during error-driven learning. *Neuron* **106**, 329–339 (2020).

34. Steinmetz, N. A., Zatka-Haas, P., Carandini, M. & Harris, K. D. Distributed coding of choice, action and engagement across the mouse brain. *Nature* **576**, 266–273 (2019).

35. Stringer, C. *et al.* Spontaneous behaviors drive multidimensional, brainwide activity. *Science* **364**, (2019).

36. Musall, S., Kaufman, M. T., Juavinett, A. L., Gluf, S. & Churchland, A. K. Single-trial neural dynamics are dominated by richly varied movements. *Nature neuroscience* **22**, 1677–1686 (2019).

37. Hoang, H. *et al.* Improved hyperacuity estimation of spike timing from calcium imaging. *Sci Rep* **10**, 17844 (2020).

38. Rupprecht, P. *et al. Database and deep learning toolbox for noise-optimized, generalized spike inference from calcium imaging*. http://biorxiv.org/lookup/doi/10.1101/2020.08.31.272450 (2020) doi:10.1101/2020.08.31.272450.

39. Sebastian, J., Sur, M., Murthy, H. A. & Magimai-Doss, M. Signal-to-signal neural networks for improved spike estimation from calcium imaging data. *PLoS Comput Biol* **17**, e1007921 (2021).

40. Dechery, J. B. & MacLean, J. N. Functional triplet motifs underlie accurate predictions of single-trial responses in populations of tuned and untuned V1 neurons. *PLoS computational biology* **14**, e1006153 (2018).

41. Kirschbaum, E. *et al.* LeMoNADe: Learned Motif and Neuronal Assembly Detection in calcium imaging videos. *arXiv:1806.09963 [q-bio]* (2019).

42. Mackevicius, E. L. *et al.* Unsupervised discovery of temporal sequences in high-dimensional datasets, with applications to neuroscience. *eLife* **8**, e38471 (2019).

43. Triplett, M. A., Pujic, Z., Sun, B., Avitan, L. & Goodhill, G. J. Model-based decoupling of evoked and spontaneous neural activity in calcium imaging data. *PLoS Comput Biol* **16**, e1008330 (2020).

44. Williams, A. H. *et al.* Unsupervised Discovery of Demixed, Low-Dimensional Neural Dynamics across Multiple Timescales through Tensor Component Analysis. *Neuron* **98**, 1099-1115.e8 (2018).

45. Wu, A., Pashkovski, S., Datta, S. R. & Pillow, J. W. Learning a latent manifold of odor representations from neural responses in piriform cortex. in *Advances in Neural Information Processing Systems* (eds. Bengio, S. et al.) vol. 31 (Curran Associates, Inc., 2018).

46. Costa, A. C., Ahamed, T. & Stephens, G. J. Adaptive, locally linear models of complex dynamics. *Proc Natl Acad Sci USA* **116**, 1501–1510 (2019).

47. Glaser, J., Whiteway, M., Cunningham, J. P., Paninski, L. & Linderman, S. Recurrent Switching Dynamical Systems Models for Multiple Interacting Neural Populations. in *Advances in Neural Information Processing Systems* (eds. Larochelle, H., Ranzato, M., Hadsell, R., Balcan, M. F. & Lin, H.) vol. 33 14867–14878 (Curran Associates, Inc., 2020).

48. Picardo, M. A. *et al.* Population-Level Representation of a Temporal Sequence Underlying Song Production in the Zebra Finch. *Neuron* **90**, 866–876 (2016).

49. Mano, O. *et al.* Using slow frame rate imaging to extract fast receptive fields. *Nature communications* **10**, 1–13 (2019).

50. Prince, L. Y., Bakhtiari, S., Gillon, C. J. & Richards, B. A. *Parallel inference of hierarchical latent dynamics in two-photon calcium imaging of neuronal populations*. http://biorxiv.org/lookup/doi/10.1101/2021.03.05.434105 (2021) doi:10.1101/2021.03.05.434105.

51. Minderer, M., Brown, K. D. & Harvey, C. D. The spatial structure of neural encoding in mouse posterior cortex during navigation. *Neuron* **102**, 232–248 (2019).

52. Sofroniew, N. J., Flickinger, D., King, J. & Svoboda, K. A large field of view two-photon mesoscope with subcellular resolution for in vivo imaging. *Elife* **5**, e14472 (2016).

53. Jaderberg, M. *et al.* Population Based Training of Neural Networks. *arXiv:1711.09846 [cs]* (2017).

54. Dana, H. *et al.* High-performance calcium sensors for imaging activity in neuronal populations and microcompartments. *Nat Methods* **16**, 649–657 (2019).

55. Art, J. Photon detectors for confocal microscopy. in *Handbook of biological confocal microscopy* 251–264 (Springer, 2006).

56. Starck, J.-L., Murtagh, F. D. & Bijaoui, A. *Image processing and data analysis: the multiscale approach*. (Cambridge University Press, 1998).

525 57. Vogelstein, J. T. *et al.* Fast Nonnegative Deconvolution for Spike Train Inference From Population Calcium
526   Imaging. *Journal of Neurophysiology* **104**, 3691–3704 (2010).
527 58. Heikkila, J. & Silvén, O. A four-step camera calibration procedure with implicit image correction. in
528   *Proceedings of IEEE computer society conference on computer vision and pattern recognition* 1106–1112
529   (IEEE, 1997).
530 59. Zhang, Z. A flexible new technique for camera calibration. *IEEE Transactions on pattern analysis and*
531   *machine intelligence* **22**, 1330–1334 (2000).

532

Methods

AutoLFADS and RADICaL architecture and training

The core model that AutoLFADS and RADICaL build on is LFADS. A detailed overview of the LFADS model is given in refs. [15,16]. Briefly, LFADS is a sequential application of a variational auto-encoder (VAE). A pair of bidirectional RNNs (the initial condition and controller input encoders) operate on the spike sequence and produce initial conditions for the generator RNN and time-varying inputs for the controller RNN. All RNNs were implemented using gated recurrent unit (GRU) cells. At each time step, the generator state evolves with input from the controller and the controller receives delayed feedback from the generator. The generator states are linearly mapped to factors, which are mapped to the firing rate of the neurons using a linear mapping followed by an exponential nonlinearity. The optimization objective is to maximize a lower bound on the likelihood of the observed spiking activity given the rates produced by the generator network, and includes KL and L2 regularization penalties. During training, network weights are optimized using stochastic gradient descent and backpropagation through time.

Identical network sizes were used for both AutoLFADS and RADICaL runs and for both simulation and real 2P data. The dimension of initial condition encoder, controller input encoder, and controller RNNs was 64. The dimension of the generator RNN was 100. The generator was provided with 64-dimensional initial conditions and 2-dimensional controller outputs (i.e., inferred inputs u(t)) and linearly mapped to 100-dimensional factors. The initial condition prior distribution was Gaussian with a trainable mean that was initialized to 0 and a variance that was fixed to 0.1. The minimum allowable variance of the initial condition posterior distribution was set to 1e-4. The controller output prior was autoregressive with a trainable autocorrelation tau and noise variance, initialized to 10 and 0.1, respectively. The Adam optimizer (epsilon: 1e-8; beta1: 0.9; beta2: 0.99; initial learning rate: 1e-3, **Table 1**) was used to control weight updates.The loss was scaled by a factor of 1e4 prior to computing the gradients for numerical stability. To prevent potential pathological training, the GRU cell hidden states were clipped at 5 and the global gradient norm was clipped at 300.

AutoLFADS is a recent implementation of the population based training (PBT) approach[53] on LFADS to perform automatic, large-scale hyperparameter (HP) search. A detailed overview of AutoLFADS is in refs. [17,21]. Briefly, PBT distributes training across dozens of models in parallel, and uses evolutionary algorithms to tune HPs over many generations. At the end of each generation, a selection process was performed to choose higher performing models and replace the poor models with the higher performing models. The HPs of the higher performing models were perturbed before the next generation to increase the HP search space. After many generations (~30-150), the PBT process converges upon a high performing model with optimized HPs.

Twenty LFADS models were trained in parallel for 50 epochs per generation for both AutoLFADS and RADICaL runs and for both simulation and real 2P data. KL and L2 regularization penalties were linearly ramped for the first 80 epochs of training during the first generation. Training was stopped when there was no improvement in performance after 25 generations. The HPs optimized by PBT were the model's learning rate and six regularization HPs: scaling weights for the L2 penalties on the generator, controller, and initial condition encoder RNNs, scaling weights for the KL penalties on the initial conditions and controller outputs, and two dropout probabilities ("keep ratio" for coordinated dropout[21]; and RNN network dropout probability). The HP search ranges are detailed in **Table 1**. The magnitudes of the HP perturbation were controlled by weights and specified for different HPs (a weight of 0.3 results in perturbation factors between 0.7 and 1.3; **Table 1**). The learning rate and dropout probabilities were restricted to their specified search ranges and were sampled from uniform distributions. The KL and L2 HPs were sampled from log-uniform distributions and could be perturbed outside of the initial search ranges. Identical hyperparameter settings were used for both RADICaL and AutoLFADS and for both synthetic datasets and real 2P datasets.

577

578 RADICaL is an adaptation of AutoLFADS for 2P calcium imaging. RADICaL operates on sequences of deconvolved calcium
579 events x(t). x(t) are modeled as a noisy observation of an underlying time-varying Zero-Inflated Gamma (ZIG) distribution[22]:

580

581 $$x_n(t) \sim (1 - q_n(t)) \cdot \delta(0) + q_n(t) \cdot gamma(\alpha_n(t), k_n(t), loc_n),$$

582

583 where $x_n(t)$ is the distribution of observed deconvolved events, $a_n(t)$, $k_n(t)$, and loc_n are the scale, shape, and location
584 parameters, respectively, of the gamma distribution, and $q_n(t)$ denotes the probability of non-zeros, for neuron n at time t.
585 loc_n was fixed as the minimum nonzero deconvolved event (s_{min}). In the original AutoLFADS model, factors were mapped to
586 a single time-varying parameter for each neuron (the Poisson firing rate) via a linear transformation followed by an
587 exponential nonlinearity. RADICaL instead infers the three time-varying parameters for each neuron, $a_n(t)$, $k_n(t)$, and $q_n(t)$,
588 by linearly transforming the factors followed by a trainable scaled sigmoid nonlinearity (sig_n). sig_n is a positive parameter that
589 scales the outputs of the sigmoid to be in a range between 0 and sig_n, and is optimized alongside network weights. An L2
590 penalty is applied between sig_n and a PBT-searchable prior (**Table 1**) to prevent extreme values. The training objective is to
591 minimize the negative log-likelihood of the deconvolved events given the inferred parameters:

592

593 $$\prod p(x_n(t)|\text{ZIG}(\hat{\alpha_n}(t), \hat{k_n}(t), \hat{q_n}(t)))$$

594

595 The event rate for neuron n at time t was estimated by taking the mean of the inferred ZIG distribution:

596

597 $$\hat{q_n}(t) \cdot (\hat{k_n}(t) \cdot \hat{\alpha_n}(t) + s_{min})$$

598

599 RADICaL uses an SBTT training strategy to achieve subframe modeling resolution. RADICaL operates on binned
600 deconvolved calcium events, with bin size smaller than the frame timebase of imaging. Bins where the neurons were sampled
601 were filled with the corresponding event rates, while bins where the neurons were not sampled were filled with NaNs. The
602 networks still output the time-varying ZIG distribution at each timestep; however, a mask was applied to the timesteps where
603 the NaN samples were to prevent the cost computed from these timesteps being backpropagated during gradient calculation.
604 As a result, the model weights were only updated based on the cost at the sampled timesteps. The reconstruction cost also
605 excluded the cost calculated at the non-sampled timesteps so the PBT model selection was not affected by the cost
606 computed from the non-sampled timesteps.

607

608 **Simulation experiments.**
609 *Generating spike trains from an underlying Lorenz system*
610 Synthetic data were generated using the Lorenz system as described in the original LFADS work[15,16]. Lorenz parameters
611 were set to standard values (σ: 10, ρ: 28, and β: 8/3), and Δt was set to 0.01. Datasets with different speeds of dynamics
612 were generated by downsampling the original generated Lorenz states by different factors. The speed of the Lorenz
613 dynamics was quantified based on the peak location of the power spectra of the Lorenz Z dimension, with a sampling
614 frequency of 100 Hz. The downsampling factors were 3, 5, 7, 9, 11 and 14 for speeds 4, 7, 10, 13, 15 and 20 Hz, respectively.
615 Each dataset/speed consisted of 8 conditions, with 60 trials per condition. Each condition was obtained by starting the Lorenz
616 system with a random initial state vector and running it for 900 ms. The trial length for the 4 Hz dataset was longer (1200
617 ms) than that of other datasets (900 ms) to ensure that all conditions had significant features to be modeled - with shorter
618 windows, the extremely low frequency oscillations caused the Lorenz states for some conditions to have little variance across
619 the entire window, making it trivial to approximate the essentially flat firing rates. We simulated a population of 278 neurons
620 with firing rates given by linear readouts of the Lorenz state variables using random weights, followed by an exponential
621 nonlinearity. Scaling factors were applied so the baseline firing rate for all neurons was 3 spikes/sec. Each bin represents
622 10 ms and an arbitrary frame time was set to be 30 ms (i.e., one "imaging frame" takes 3 bins). Spikes from the firing rates
623 were then generated by a Poisson process.

624

625 *Generating fluorescence signals from synthetic spike trains*

626   Realistic fluorescence signals were generated from the spike trains by convolving them with a kernel for an autoregressive
627   process of order 2 and passing the results through a nonlinearity that matched values extracted from the literature for the
628   calcium indicator GCaMP6f[3,54] (**Supp Fig. 2a & b**). Three noise sources were added to reproduce variability present in real
629   data[55–57]: Gaussian noise to the size of the calcium spike, and Gaussian and Poisson noise to the final trace (**Supp Fig. 2a**
630   **& b**). This fluorescence generation process was realized as follows: First, spike trains s(t) were generated from the Lorenz
631   system as mentioned above. Independent Gaussian noise (sd = 0.1) was added to each spike in the spike train to model
632   the variability in spike amplitude. Next, we modeled the calcium concentration dynamics c(t) as an autoregressive process
633   of order 2:

$$c(t) = \gamma_1 c(t-1) + \gamma_2 c(t-2) + s(t)$$

637   with s(t) representing the number of spikes at time t. The autoregressive coefficients γ_1 and γ_2 were computed based on the
638   rise time, decay time (τ_{on} = 20 ms, τ_{off} = 400 ms for GCaMP6f) of the calcium indicators, and the sampling frequency. Note
639   that while there is substantial variability in taus across neurons in real data[3], selecting and mimicking this variability was not
640   relevant in our work, because we compared the methods (i.e., RADICaL, AutoLFADS, and s-deconv) after deconvolution.
641   The calcium concentration dynamics were further normalized so that the peak height of the calcium dynamics generated
642   from a single spike equalled one, regardless of the sampling frequency. Subsequently, we computed the noiseless
643   fluorescence signals by passing the calcium dynamics through a nonlinear transformation estimated from the literature[54] for
644   the calcium indicator GCaMP6f (**Supp Fig. 2c & d**). After the nonlinear transformation, the relationship between spike size
645   and trace size was corrupted, and therefore we assumed the baseline of fluorescence signals to be zero and the signals
646   were rescaled to the range in [0,1] using min-max normalization. Finally, Gaussian noise (~N(0,sn)) and Poisson noise
647   (simulated as gaussian with mean 0 and variance proportional to the signal amplitude at each time point via a constant *d*)
648   were added to the normalized traces. The resulting fluorescence traces had the same sampling frequency as the synthetic
649   spike trains (100 Hz).

651   A crucial parameter is the noise level associated with each fluorescence trace. High noise levels lead to very poor spike
652   detection and very low noise levels enable a near-perfect reconstruction of the spike train. In order to select a realistic level
653   of noise we matched the correlations between real and inferred spike trains of the simulated data to those typically
654   observed[10]. We found that a truncated normal distribution of noise level for Gaussian and Poisson noise best matched the
655   correlations. More specifically, for each neuron, *sn=d* was sampled independently from a truncated normal distribution
656   N(0.12, 0.02) truncated below 0.06. With the above noise setting, the mean correlation coefficient *r* between the deconvolved
657   events and ground truth spikes was 0.32, which is consistent with the standard results reported in the spikefinder paper[10]
658   for OASIS. It is worth stressing that real data feature a broad range of noise levels that depend on the imaging conditions,
659   depth, expression level, laser power and other factors. Here we did not attempt to investigate all possible noise conditions,
660   but instead, we aimed to create a simulation with known latent variables (i.e., low-dimensional factors and event rates) that
661   reasonably approximated realistic signal-to-noise levels, in order to provide a tractable test case to compare RADICaL to
662   other methods before attempting comparisons on real data.

664   *Recreating variability in sampling times due to 2p laser scanning*
665   The fluorescence traces were simulated at 100 Hz as mentioned above. A subsampling step was then performed with
666   sampling times for each neuron staggered in time to simulate the variability in sampling times due to 2p laser scanning (as
667   in **Fig. 1e**). This produced fluorescence traces where individual neurons were sampled at 33.3 Hz, with phases of 0, 11, 22
668   ms based on each neuron's location (top, middle and bottom of the FOV, respectively). To break this down, each neuron
669   was sparsely sampled every three time points and the relative sampled times between neurons were fixed. For example, in
670   trial 1, neuron 1 was sampled at time points 1, 4, 7, … and neuron 2 was sampled at time points 2, 5, 8, …; in trial 2, neuron
671   1 was sampled at time points 2, 5, 8, … and neuron 2 was sampled at time points 3, 6, 9, … . Thus, the sampling frequency
672   for each individual neuron was 33.3 Hz, while the sampling frequency for the population was retained at 100 Hz by filling the
673   non-sampled time points with NaNs. The resulting 33.3 Hz simulated fluorescence signals for each individual neuron (i.e.,
674   with NaNs excluded) were deconvolved using OASIS[25] (as implemented in CaImAn[26]) using an auto-regressive model of
675   order 1 with s_{min} of 0.1.

677 *Data preparation for each method*
678 Four methods (RADICaL, AutoLFADS, s-deconv and s-sim-fluor) were compared by their performance on recovering the
679 ground truth latent states across different datasets/speeds. Trials (480 total for each simulated dataset) were split into 80/20
680 training and validation sets for modeling AutoLFADS and RADICaL. To prepare data for non-RADICaL methods, non-
681 sampled bins were removed so all the sampled bins were treated as if they were sampled at the same time and each bin
682 then represented 30 ms (i.e., sampling frequency = 33.3 Hz). Preparing the data for AutoLFADS required discretizing the
683 deconvolved events into spike count estimates, because AutoLFADS was primarily designed to model discrete spiking data.
684 In the discretizing step, if the event rate was 0, it was left as 0; if the event rate was between 0 and 2, it was cast to 1 (to
685 bias toward the generally higher probability of fewer spikes). If the event rate was greater than 2, it was rounded down to
686 the nearest integer. We note that this is one of many possible patches to convert continuously-valued event intensities to
687 natural numbers for compatibility with the Poisson distribution and AutoLFADS; a more principled solution would be to modify
688 the network to use the ZIG distribution, as we have done in RADICaL. With s-deconv, the deconvolved events were
689 smoothed by convolution with a Gaussian filter (6 ms s.d.) to produce event rates. With s-sim-fluor, the generated
690 fluorescence signals were smoothed by convolution with a Gaussian filter (6 ms s.d.) to produce event rates. The choice of
691 filter width was optimized by sweeping values ranging from 3 to 40 ms. Smoothing with a 6 ms s.d. filter gave the highest
692 performance in recovering the ground truth Lorenz states for experiments with higher Lorenz frequencies (i.e., >= 10 Hz).
693 The event rates produced from RADICaL had a sampling frequency of 100 Hz, while the event rates produced from the non-
694 RADICaL methods had a sampling frequency of 33.3 Hz. The non-RADICaL rates were then resampled at 100 Hz using
695 linear interpolation.
696

697 *Mapping to ground truth Lorenz states*
698 Since our goal was to quantify modeling performance by estimating the underlying Lorenz states, we trained a mapping from
699 the output of each model (i.e., the event rates) to the ground truth Lorenz states using ridge regression. First, we split the
700 trials into training (80%) and test (20%) sets. We used the training set to optimize the regularization coefficient using 5-fold
701 cross-validation, and used the optimal regularization coefficient to train the mapping on the full training set. We then
702 quantified state estimation performance by applying this trained mapping to the test set and calculating the coefficient of
703 determination (R^2) between the true and predicted Lorenz states. We repeated the above procedure five times with train/test
704 splits drawn from the data in an interleaved fashion. We reported the mean R^2 across the repeats, such that all reported
705 numbers reflect held-out performance. We tested whether the difference of R^2 between each pair of methods was significant
706 by performing a paired, one-sided Student's t-test on the distribution of R^2 across the five folds of predictions.
707

708 **Real 2p experiments**
709 *Surgical procedures*
710 All procedures were approved by the University of Chicago Animal Care and Use Committee. Two male Ai148D transgenic
711 mice (TIT2L-GC6f-ICL-tTA2, stock 030328; Jackson Laboratory) were used. Each mouse underwent a single surgery. Mice
712 were injected subcutaneously with dexamethasone (8 mg/kg) 24 hours and 1 hour before surgery. Mice were anesthetized
713 with 2-2.5% inhaled isoflurane gas, then injected intraperitoneally with a ketamine-medetomidine solution (60 mg/kg
714 ketamine, 0.25 mg/kg medetomidine), and maintained on a low level of supplemental isoflurane (0-1%) if they showed any
715 signs that the depth of anesthesia was insufficient. Meloxicam was also administered subcutaneously (2 mg/kg) at the
716 beginning of the surgery and for 1-3 subsequent days. The scalp was shaved, cleaned, and resected, the skull was cleaned
717 and the wound margins glued to the skull with tissue glue (VetBond, 3M), and a 3 mm circular craniotomy was made with a
718 3 mm biopsy punch centered over the left CFA/S1 border. The coordinates for the center of CFA were taken to be 0.4 mm
719 anterior and 1.6 mm lateral of bregma. The craniotomy was cleaned with SurgiFoam (Ethicon) soaked in phosphate-buffered
720 solution (PBS), then virus (AAV9-CaMKII-Cre, stock $2.1*10^{13}$ particles/nL, 1:1 dilution in PBS, Addgene) was pressure
721 injected (NanoJect III, Drummond Scientific) at two or four sites near the target site, with 140 nL injected at each of two
722 depths per site (250 and 500 µm below the pia) over 5 minutes each. The craniotomy was then sealed with a custom
723 cylindrical glass plug (3 mm diameter, 660 µm depth; Tower Optical) bonded (Norland Optical Adhesive 61, Norland) to a 4
724 mm #1 round coverslip (Harvard Apparatus), glued in place first with tissue glue (VetBond) and then with cyanoacrylate glue
725 (Krazy Glue) mixed with dental acrylic powder (Ortho Jet; Lang Dental). A small craniotomy was also made using a dental
726 drill over right CFA at 0.4 mm anterior and 1.6 mm lateral of bregma, where 140 nL of AAVretro-tdTomato (stock $1.02*10^{13}$
727 particles/nL, Addgene) was injected at 300 µm below the pia. This injection labeled cells in left CFA projecting to the
728 contralateral CFA. Here, this labeling was used solely for stabilizing the imaging plane (see below). The small craniotomy

729 was sealed with a drop of Kwik-Cast (World Precision Instruments). Two layers of MetaBond (C & B) were applied, then a
730 custom laser-cut titanium head bar was affixed to the skull with black dental acrylic. Animals were awoken by administering
731 atipamezole via intraperitoneal injection and allowed to recover at least 3 days before water restriction.
732

733 *Behavioral task*
734 The behavioral task (Fig. 3a) was a variant of the water reaching task of ref. [27] which we term the "Water Grab" task. This
735 task was performed by water-restricted, head-fixed mice, with the forepaws beginning on paw rests (eyelet screws) and the
736 hindpaws and body supported by a custom 3D printed clear acrylic tube enclosure. After holding the paw rests for 700-900
737 ms, a tone was played by stereo speakers and a 2-3 μL droplet of water appeared at one of two water spouts (22 gauge,
738 90-degree bent, 1" blunt dispensing needles, McMaster) positioned on either side of the snout. The pitch of the tone indicated
739 the location of the water, with a 4000 Hz tone indicating left and a 7000 Hz tone indicating right, and it lasted 500 ms or until
740 the mouse made contact with the correct water spout. The mouse could grab the water droplet and bring it to its mouth to
741 drink any time after the tone began. Both the paw rests and spouts were wired with capacitive touch sensors (Teensy 3.2,
742 PJRC). Good contact with the correct spout produced an inter-trial interval of 3-6 s, while failure to make contact (or
743 insufficiently strong contact) with the spout produced an inter-trial interval of 20 s. Because the touch sensors required good
744 contact from the paw, this setup encouraged complex contacts with the spouts. The mice were trained to make all reaches
745 with the right paw and to keep the left paw on the paw rest during reaching. Training took approximately two weeks, though
746 the behavior continued to solidify for at least two more weeks. Data presented here were collected after 6-8 weeks'
747 experience with the task. Control software was custom written in MATLAB R2018a using PsychToolbox 3.0.14, and for the
748 Teensy. Touch event monitoring and task control were performed at 60 Hz.
749

750 Behavior was also recorded using a pair of cameras (BFS-U3-16S2M-CS, FLIR; varifocal lenses COZ2813CSIR2,
751 Computar) mounted 150 mm from the right paw rest at 10° apart to enable 3D triangulation. Infrared illuminators enabled
752 behavioral imaging while performing 2p imaging in a darkened microscope enclosure. Cameras were synchronized and
753 recorded at 150 frames per second with real-time image cropping and JPEG compression, and streamed to one HDF5 file
754 per camera (areaDetector module of EPICS, CARS). The knuckles and wrist of the reaching paw were tracked in each
755 camera using DeepLabCut and triangulated into 3D using camera calibration parameters obtained from the MATLAB Stereo
756 Camera Calibration toolbox[58,59]. To screen the tracked markers for quality we created distributions of all inter-marker
757 distances in 3D across every labeled frame and identified as problematic frames with any inter-marker distance exceeding
758 the 99.9th percentile of its respective distribution. Trials with more than one problematic frame in the period of -200 ms to
759 800 ms after the raw reach onset were discarded (where reach onset was taken as the first 60 Hz tick after the paw rest
760 touch sensor fell below contact threshold). The kinematics of all trials that passed this screening procedure were visualized
761 to confirm quality. Centroid marker kinematics were obtained by averaging the kinematics of all paw markers, locking them
762 to behavioral events and then smoothing using a Gaussian filter (15 ms s.d.). To obtain velocity and acceleration, centroid
763 data was numerically differentiated with MATLAB's *diff* function and then smoothed again using a Gaussian filter (15 ms
764 s.d.).
765

766 *Two-photon imaging*
767 Calcium imaging was performed with a Neurolabware two-photon microscope and pulsed Ti:sapphire laser (Vision II,
768 Coherent). Depth stability of the imaging plane was maintained using a custom plugin that acquired an image stack at the
769 beginning of the session (1.4 μm spacing), then compared a registered rolling average of the red-channel data to each plane
770 of the stack. If sufficient evidence indicated that a plane not at the center of the stack was a better match to the image being
771 acquired, the objective was automatically moved to compensate. This typically resulted in a slow and steady upward
772 (outward) movement of the objective over the course of the session.
773

774 Offline, images were run through Suite2p to perform motion correction, region-of-interest (ROI) detection, and fluorescence
775 extraction from both ROIs and neuropil. ROIs were manually curated using the Suite2p GUI to retain only those
776 corresponding to somas. We then subtracted the neuropil signal scaled by 0.7[23]. Neuropil-subtracted ROI fluorescence was
777 then detrended by performing a running 10th percentile operation, smoothing with a Gaussian filter (20 s s.d.), then
778 subtracting the result from the trace. This result was fed into OASIS[25] using the 'thresholded' method, AR1 event model, and
779 limiting the tau parameter to be between 300 and 800 ms. Neurons were discarded if they did not meet a minimum signal-
780 to-noise (SNR) criterion. To compute SNR, we took the fluorescence at each time point when OASIS identified an "event"

781   (non-zero), computed (fluorescence - neuropil) / neuropil, and computed the median of the resulting distribution. ROIs were
782   excluded if this value was less than 0.05. To put events on a more useful scaling, for each ROI we found the distribution of
783   event sizes, smoothed the distribution (ksdensity in MATLAB, with an Epanechnikov kernel and log transform), found the
784   peak of the smoothed distribution, and divided all event sizes by this value. This rescales the peak of the distribution to have
785   a value of unity. Data from two mice and two brain areas (4 sessions in total) were used (Mouse1 M1: 510 neurons, 560
786   trials; Mouse1 S1: 433 neurons, 502 trials; Mouse2 M1: 439 neurons, 475 trials; Mouse2 S1: 509 neurons, 421 trials).
787

788   *Data preparation for modeling with RADICaL and AutoLFADS*
789   To prepare data for RADICaL, the deconvolved events were normalized by the s_min value output by OASIS so that the
790   minimal event size was 0.1 across all neurons. The deconvolved events for individual neurons had a sampling rate equal to
791   the frame rate (31.08 Hz). For modeling with RADICaL, the deconvolved events were assigned into 10ms bins using the
792   timing of individual measurements for each neuron to achieve sub-frame resolution (i.e., 100 Hz). The non-sampled bins
793   were filled with NaNs. To prepare data for AutoLFADS, the deconvolved events were rescaled using the distribution-scaling
794   method described above, and casted using the casting step described in the simulation section. For both AutoLFADS and
795   s-deconv, the deconvolved events were assigned into a single time bin per frame (i.e., 32.17 ms bins) to mimic standard
796   processing of 2p imaging data, where the sub-frame timing of individual measurements is discarded. Trials were created by
797   aligning the data to 200 ms before and 800 ms after reach onset (100 time points per trial for RADICaL, and 31 time points
798   per trial for AutoLFADS and s-deconv). An individual RADICaL model and AutoLFADS model were trained for each dataset
799   (4 total). Failed trials (latency to contact with correct spout > 15 s for Mouse1, 20 s for Mouse2), or trials where the grab to
800   the incorrect spout occurred before the grab to the correct spout, were discarded. For each dataset, trials (Mouse1 M1: 552
801   total; Mouse1 S1: 500 total; Mouse2 M1: 467 total; Mouse2 S1: 413 total) were split into 80/20 training and validation.
802

803   *Trial grouping*
804   PSTH analysis and low dimensional neural trajectory visualization were performed based on subgroups of trials. Trials were
805   sorted into two subgroups per spout based on the Z dimension (height) of hand position. The hand position was obtained by
806   smoothing the centroid marker position with a Gaussian filter (40 ms s.d.). Time windows where the height of hand was used
807   to split trials were hand-selected to present a good separation between subgroups of hand trajectories. For mouse1 M1, a
808   window of 30 ms to 50 ms after reach onset was used to split left condition trials and a window of 180 ms to 200 ms after
809   reach onset was used to split right condition trials; for mouse1 S1, a window of 180 ms to 200 ms after reach onset was
810   used to split left condition trials and a window of 140 ms to 160 ms after reach onset was used to split right condition trials;
811   for both mouse2 M1 and mouse2 S1, a window of 30 ms to 50 ms after reach onset was used to split both left and right
812   condition trials. For both left or right conditions and for all mice/areas (with the exception of mouse1 M1), 55 trials with the
813   lowest and highest heights were selected as group 1 and group 2, respectively; trials with middle-range heights were
814   discarded. For mouse1 M1, the first 25 trials with the lowest heights for right condition were discarded because these reaches
815   were highly non-stereotyped and loopy; instead, the 26th to 80th trials with the lowest heights were selected as group 1 for
816   the right condition.
817

818   *PSTH analysis and comparing RADICaL and AutoLFADS single-trial rates*
819   RADICaL was first validated by comparing the PSTHs computed using RADICaL inferred event rates and the empirical
820   PSTHs. Empirical PSTHs were computed by trial-averaging s-deconv rates (40 ms kernel s.d., 32.17 ms bins) within each
821   of the 4 subgroups of trials. RADICaL inferred rates were first downsampled from 100 Hz to 31.08 Hz with an antialiasing
822   filter applied, to match the sampling frequency (i.e., the frame rate) of the original deconvolved signals. RADICaL PSTHs
823   were computed by similarly averaging RADICaL rates. Single-trial inferred rates were then compared to the empirical PSTHs
824   to assess how well each method recapitulated the empirical PSTHs on single trials. The correlation coefficient (r) was
825   computed between inferred single-trial event rates and the corresponding empirical PSTHs in a cross-validated fashion, i.e.,
826   each trial's inferred event rate was compared against an empirical PSTH computed using all other trials within the subgroup.
827   *r* was assessed for the time window spanning 200 ms before to 800 ms after reach onset, and computed by concatenating
828   all trials across the four subgroups, yielding one *r* for each neuron. Neurons that had fewer than 40 nonzero events within
829   this time window (across all trials) were excluded from the analysis.
830

831   *Low-D analysis*

832 To visualize the low-dimensional neural trajectories that RADICaL produced, principal component analysis (PCA) was
833 performed on RADICaL inferred rates. RADICaL rates (aligned to 200 ms before and 800 ms after reach onset) were log-
834 transformed (with 1e-4 added to prevent numerical precision issues) and normalized to have zero mean and unit standard
835 deviation for each neuron. PCA was applied to the trial-averaged rates and the projection matrix was then used to project
836 the log-transformed and normalized single-trial rates (aligned to 200 ms before and 400 ms after reach onset) onto the top
837 3 PCs.

838
839 *Decoding analysis*
840 RADICaL-inferred rates, AutoLFADS-inferred rates, and s-deconv (Gaussian kernel 40 ms s.d.) rates were used to decode
841 hand position and velocity using ridge regression. The hand position and velocity were obtained as described above and
842 binned at 10 ms (i.e., 100 Hz). The non-RADICaL rates were retained to a sampling frequency of 100 Hz using linear
843 interpolation. For simplicity, we did not include a lag between the neural data and kinematics. However, additional analyses
844 confirmed that adding a lag did not alter the results (data not shown). Trials with an interval between water presentation and
845 reach onset that was longer than a threshold were discarded due to potential variations in behavior (e.g., inattention). The
846 threshold was selected arbitrarily for different sessions based on the actual distribution of the intervals in the session (Mouse1
847 M1: 500 ms; Mouse1 S1: 400 ms; Mouse2 M1: 400 ms; Mouse2 S1: 600 ms). The data were aligned to 50 ms before and
848 350 ms after reach onset. The decoder was trained and tested using cross-validated ridge regression. First, we split the
849 trials into training (80%) and test (20%) sets. We used the training set to optimize the regularization coefficient using 5-fold
850 cross-validation, and used the optimal regularization coefficient to train the decoder on the full training set. This trained
851 decoder was applied to the test set, and the coefficient of determination (R^2) was computed and averaged across x-, y- and
852 z- kinematics. We repeated the above procedure five times with train/test splits drawn from the data in an interleaved fashion.
853 We reported the mean R^2 across the repeats, such that all reported numbers reflect held-out performance. We tested
854 whether the difference of R^2 between each pair of methods was significant by performing paired, one-sided Student's t-Test
855 on the distribution of R^2 across the five folds of predictions.

856
857 *Coherence analysis*
858 Coherence was computed between the true and predicted kinematics (window: 200 ms before and 500 ms after reach onset)
859 across all trials and across all x-, y- and z- dimensions using magnitude-squared coherence (MATLAB: mscohere). The
860 power spectral density estimation parameters within mscohere were specified to ensure a robust calculation on the single
861 trial activity: Hanning windows with 35 timesteps (i.e., 350 ms) for the FFT and window size, and 25 timesteps (i.e., 250 ms)
862 of overlap between windows.

863
864 *t-SNE analysis on the weights mapping from factors to ZIG parameters*
865 RADICaL relies on subframe bins in which neurons are grouped based on their spatial locations within the FOV. Because
866 this strategy results in consistent neuron grouping, it could potentially result in different groups of neurons corresponding to
867 different latent factors. To test whether such an artifact existed, we visualized the transformation from latents to neurons by
868 using t-SNE to reduce the 300-dimensional weights vector (100 factors * 3 ZIG parameters) into a 2-D t-SNE space for each
869 individual neuron (510 neurons total) (**Supp. Fig. 9**). We did not observe a relationship between neurons' position within the
870 field of view (i.e., top, middle, and bottom) and the underlying factors. This suggested that the model did not use distinct
871 factors for sets of neurons that were sampled with different phases, despite neurons in distant portions of the FOV never
872 being grouped in the same bin.

873
874 *Neuron downsampling*
875 The neuron downsampling experiment was performed on the Mouse2 M1 dataset. The number of neurons included when
876 training RADICaL or AutoLFADS was gradually reduced by limiting the area of FOV that the neurons were sampled from.
877 The area was shrunk from the entire FOV with an area-to-FOV ratio of 1, 25/36, 9/16, 1/4, and 1/9, resulting in the number
878 of included neurons to be 439, 321, 262, 121 and 59. An individual RADICaL model and AutoLFADS model were trained for
879 each number of neurons. Decoding was performed using ridge regression (see above).

880
881
882
883

			LR	CD	DO	KL CO	KL IC	L2 Con	L2 Gen	Sig Prior
Defaults	RADICaL	Ranges	(1e-5, 5e-3)	(0.01, 0.99)	(0.3, 1.0)	(1e-6, 1e-4)	(1e-6, 1e-4)	(1e-5, 0.1)	(1e-5, 0.1)	(1.0, 100.0)
		Initial values	1e-3	0.5	uniform	loguniform	loguniform	loguniform	loguniform	20.0
		Explore weight	0.3	0.3	0.3	0.8	0.8	0.8	0.8	0.2
		Limit explore	TRUE	TRUE	TRUE	FALSE	FALSE	FALSE	FALSE	FALSE
	AutoLFADS	Ranges	(1e-5, 5e-3)	(0.01, 0.99)	(0.3, 1.0)	(1e-6, 1e-4)	(1e-6, 1e-4)	(1e-5, 0.1)	(1e-5, 0.1)	-
		Initial values	1e-3	0.5	uniform	loguniform	loguniform	loguniform	loguniform	-
		Explore weight	0.3	0.3	0.3	0.8	0.8	0.8	0.8	-
		Limit explore	TRUE	TRUE	TRUE	FALSE	FALSE	FALSE	FALSE	-

Table 1. Hyperparameter ranges for RADICaL and AutoLFADS runs. Cells with a dash indicate "not applicable" for the method. LR is the learning rate. CD is the coordinated dropout rate (i.e., proportion of samples dropped at input). DO is the dropout probability for the RNN network. KL indicates the weight applied to the KL divergence of a posterior from its prior. CO indicates the controller output distributions and IC indicates the initial condition distributions. L2 indicates the weight applied to the Frobenius norm of the recurrent kernel of the GRU cell. Con indicates the controller GRU cell, Gen indicates the generator GRU cell, IC Enc indicates the initial condition encoder GRU cells. Sig Prior indicates the prior of the scaling factors applied to the sigmoid nonlinearity when mapping from factors to ZIG parameters.